



Full Length Article

Elucidating the tensile work hardening behaviour of precipitate containing $\text{Al}_{0.3}\text{Co}_{1.5}\text{CrFeNi}_{1.5}\text{Ti}_{0.2}$ high entropy alloy

Bushra Harun ^a, E-Wen Huang ^{b,c}, Yao-Jen Chang ^{c,d}, An-Chou Yeh ^{c,d}, Suresh Neelakantan ^{a,*}, Jayant Jain ^{a,*}

^a Department of Materials Science and Engineering, Indian Institute of Technology Delhi, Hauz Khas, New Delhi 110016, India

^b Department of Materials Science and Engineering, National Yang Ming Chiao Tung University, Hsinchu 30013, Taiwan

^c High Entropy Materials Center, National Tsing Hua University, Hsinchu, 30013, Taiwan

^d Department of Materials Science and Engineering, National Tsing Hua University, Hsinchu 30013, Taiwan

ARTICLE INFO

Keywords:

High entropy alloys
Strain hardening
Aging
Stacking faults
Orowan looping
Paired dislocations

ABSTRACT

A significant amount of work has been performed, since the last decade, on designing novel high entropy alloy (HEA) compositions. However, the effort on concluding a universal mechanism on the strain hardening behavior of these alloys with precipitates is limited. The current study is designed with an aim to comprehend the mechanical behavior of $\text{Al}_{0.3}\text{Co}_{1.5}\text{CrFeNi}_{1.5}\text{Ti}_{0.2}$ HEA in solution treated and aged conditions. The results show that the peak aged condition of sample contains two types of precipitates – B2 and L1₂ (γ') of approximately 800 nm and 40 nm size, respectively. They are found to be responsible for a significant increase in strength in aged samples than solution treated ones. Deformation was found to occur mainly by planar slip on the {111} primary slip planes. Noticeable strain hardening behavior was attributed to the formation of stacking faults (SFs) and Lomer-Cottrell (LC) locks, inhibiting the dislocation motion. Numerous paired dislocations formed due to inhibition of slip by the ordered γ' precipitates, coexist with a few Orowan loops in the peak-aged alloy after deformation. However, the primary strengthening mechanism was found to be the shearing of γ' precipitates by partial dislocations. Shearing of nanosized γ' precipitates by partial dislocations is energetically favourable for the system than shearing by full dislocations. Overall, this study enhances the understanding of the precipitation strengthening and strain hardening mechanisms in high entropy alloys.

1. Introduction

High entropy alloys (HEAs) exhibit the potential to cater to the demands of high-performance materials. HEAs are different from conventional alloys in that they are multi-principal elemental alloys with five or more elements in equiatomic or nearly equiatomic proportions. The extraordinary properties of these alloys are attributed to the four core effects: high entropy, lattice distortion, sluggish diffusion, and cocktail effect [1–5]. Exploring these materials, whose compositions lie in and around the middle of phase diagrams of multicomponent systems has proven beneficial in terms of various properties such as mechanical, refractory, magnetic, etc. [1,3,6,7]. The exceptional mechanical properties of these alloys have attracted researchers to comprehend the reason behind the unanticipated behavior and to investigate processes that would further enhance the properties of these alloy systems.

CoCrFeNi HEAs show promising properties along with Al and Ti

additions making them compelling candidates for further exploration [8,9]. $\text{AlCoCrFeNiTi}_{0.5}$ HEA possesses yield strength (2.26 GPa) and failure strain (23.3 %) values superior to most high-strength alloys, such as bulk metallic glasses [9]. The properties of these alloys can further be improved by precipitation strengthening [10]. For instance, precipitation strengthening in $\text{FeCoNiAl}_{0.4}\text{Ti}_{0.6}$ HEA contributes to a yield strength of ~1.86 GPa and an ultimate tensile strength of ~2.52 GPa, with a fracture strain of ~5.2 % [11]. Precipitation hardenability is also observed in non-equiatomic CoCrFeNi HEAs with Al/Ti additions containing a greater proportion of Co and Ni to ensure FCC phase stability [12–14].

Previous studies have shown that the formation of stacking faults (SFs), Lomer-Cottrell (LC) locks, deformation twins, Taylor lattice and high-density dislocation walls (HDDWs) contribute to the overall strain hardening behavior in various FCC-based alloys [15]. For example, in $\text{FeMnCr}_{0.25}\text{Co}_{0.25}$ HEA, deformation mechanisms such as twinning or

* Corresponding authors.

E-mail addresses: sureshn@iitd.ac.in (S. Neelakantan), jayantj@iitd.ac.in (J. Jain).

planar slip are activated in different orientations, and the formation of deformation structures such as SFs, dislocation cells, and Taylor lattices is also reported [16]. Gangireddy et al. [17] observed twinning in low stacking fault energy, single phase FCC, Al_{0.3}CoCrFeNi HEA, leading to a distinct four-stage strain hardening behavior.

In γ' strengthened FCC alloys, strain hardening mainly occurs due to precipitate shearing or bypassing of dislocations [18–20]. After the deformation of (NiCoCr)₇₆(Ni₆AlTi)₃ FCC-based medium entropy alloy (MEA), it exhibits multiple stacking faults and a Taylor lattice structure. The same MEA with L₁₂ precipitates shows the presence of numerous stacking faults and sheared particles after deformation [15]. Gwalani et al. [20] observed that precipitation of ordered L₁₂ intermetallic in Al_{0.7}CoCrFeNi results in enhanced strength. In this case, the Orowan mechanism explains the strengthening caused by fine-scale L₁₂ precipitates. The slip is the dominant deformation mode, albeit twins are observed under dynamic loading. Paired dislocations have been found very often in the Ni-based superalloys containing L₁₂ precipitates where the ordered domains act as an obstacle to the dislocation slip and thus lead to the dissociation of dislocations into Shockley partials [19,21,22]. Only a few reports are available on medium [23] and high entropy alloys that study the effect of precipitates on the hardening behavior during tensile loading. While the aging behavior of CoCrFeNi with Al/Ti additions has been extensively studied in the literature [10], there remains a notable gap in understanding their strain hardening mechanism under solutionized and aged conditions.

This paper presents a comprehensive investigation of the mechanical properties of Al_{0.3}Co_{1.5}CrFeNi_{1.5}Ti_{0.2} (Al03Ti02) alloy, including the development of a phase diagram using the Calculation of Phase Diagrams (CALPHAD) method [24]. The precipitation behavior of the alloy was studied with the help of hardness tests and microstructural analysis using field emission scanning electron microscope (FESEM). Subsequently, the tensile properties of solutionized and peak aged Al03Ti02 were evaluated, employing advanced characterization techniques such as scanning transmission electron microscopy (STEM) to gain insights into the alloy's hardening behavior and the deformation mechanisms involved under solutionized and peak-aged conditions.

2. Materials and methods

2.1. Materials

Al_{5.5}Co_{27.3}Cr_{18.2}Fe_{18.2}Ni_{27.3}Ti_{3.5} at.% (represented as Al_{0.3}Co_{1.5}CrFeNi_{1.5}Ti_{0.2} in atomic ratio, further referred to as Al03Ti02) high entropy alloy bars with dimensions of 80 mm x 80 mm x 20 mm were processed using vacuum arc melting. The raw materials with a purity greater than 99.5 at.% were melted in a vacuum of 2×10^{-2} torr under an argon atmosphere. Ti getter was utilized during the melting process to remove residual oxygen and nitrogen. The as-cast bars were subjected to a flipping and re-melting process four times to enhance the chemical homogeneity as discussed elsewhere [12]. The phase diagram for the alloy was obtained using the TCHEA5 database in Thermo-Calc 2022a software [24]. This allowed for a comprehensive understanding of the alloy's phase equilibria, solid solution regions and potential intermetallic compound formation.

2.2. Solutionizing and aging

Solutionizing of as-cast Al03Ti02 was carried out at 1150 °C for 6 h in a muffle furnace using vacuum-sealed quartz tubes at $\sim 10^{-6}$ mbar vacuum level to prevent oxidation. Aging treatments were carried out for varying lengths of time, ranging from 1 h to 1500 h at 750 °C in a tubular furnace. The selection of solutionizing and aging conditions was based on the developed phase diagrams and optimized parameters reported in the literature for similar alloys [10,12,25].

2.3. Mechanical testing

Hardness and tensile evaluations were conducted to assess the mechanical behavior of the alloy. Flat dog bone-shaped specimens with gauge dimensions of thickness-1 mm, width-3 mm, and length-12 mm were prepared using wire electrical discharge machining (EDM). Quasi-static room temperature tensile tests were performed using a 30 kN universal testing machine (UTM, ZwickRoell, Germany), equipped with an in-built video extensometer, at a strain rate of 10^{-3} s⁻¹. Minimum three tensile tests were performed for each condition. Hardening curves were determined by taking the differential of true stress-strain curve and plotting it against the true plastic stress. Hardness measurements were carried out using a Vickers microhardness tester (Shimadzu HMV, Japan) with a load of 9.81 N and a dwell time of 15 s. For each data point, the average value of at least 15 measurements taken at random spots on the surface of the sample was reported.

2.4. Microstructural characterization

X-ray diffraction (XRD) measurements were carried out to obtain the microstructural phase details using a Rigaku Ultima IV instrument operated at 40 kV with Cu K_α radiation at a scanning speed of 1° per minute. High-resolution microscopy was performed using FESEM (JEOL, JSM-7800F) to examine the microstructures of the as-cast, solutionized and aged HEA samples. Sample preparation involved mechanical polishing till 4000-grit SiC emery papers and fine polishing using 0.05 μm alumina suspension. Etching was performed using aqua regia (3 HCl:1 HNO₃) to reveal the microstructural features. Transmission electron microscopy (TEM) was conducted using a JEOL, JEM 3200FS electron microscope operated at 300 keV. Detailed deformation substructure characterization was performed using advanced STEM mode. Sample preparation for TEM involved initial mechanical polishing to 80 μm thickness, followed by twin-jet electro-polishing (Struers Tenupol 5) in a solution of 10 % perchloric acid (HClO₄) in ethanol at -30 °C at an applied voltage of 30 V.

3. Results

3.1. Initial processing involving calculated phase diagram

Fig. 1 illustrates the pseudo-binary phase diagram of the Al_xCo_{1.5}CrFeNi_{1.5}Ti_y ($x + y = 0.5$, in atomic ratio) HEA, with varying Al concentrations ranging from 0 to 9 at.%. The specific composition of the alloy investigated in this study corresponds to an Al content of 5.5 at.% ($x = 0.3$). According to the phase diagram, the alloy exhibits a single-phase FCC region (γ) at temperatures above 1050 °C. At a lower temperature of 750 °C, the phase diagram reveals the coexistence of two distinct phases, namely the B2 (β) and L₁₂ (γ') phases along with FCC phase. This observation, as a virtue of the alloy composition, deviates from previous studies on similar alloys, where either one of these precipitates was found to be stable at this temperature [10,25]. It should be noted that the different phase regimes/boundaries, temperatures/concentration predicted by Thermo-Calc may vary slightly compared to the experimental values for the same. This can potentially be attributed to the inaccuracies in the present solution thermodynamics models for these complex concentrated alloys, as have been observed in literature [26]. Nonetheless, the alloy phase diagram provides valuable insights into the stability and composition of the different phases under various temperature conditions. Understanding the phase evolution and stability of this HEA system is crucial for tailoring its microstructure and respective deformation properties for specific applications.

SEM and EDS investigations of the as-cast samples revealed the presence of Ti rich intermetallic phases, in addition to the FCC phase, as depicted in Fig. 2(a). Previous studies [25,27] have also reported the occurrence of these phases (σ and Laves phases) in the CoCrFeNi as-cast HEAs having Ti additions. The as-cast alloy was solutionized to achieve

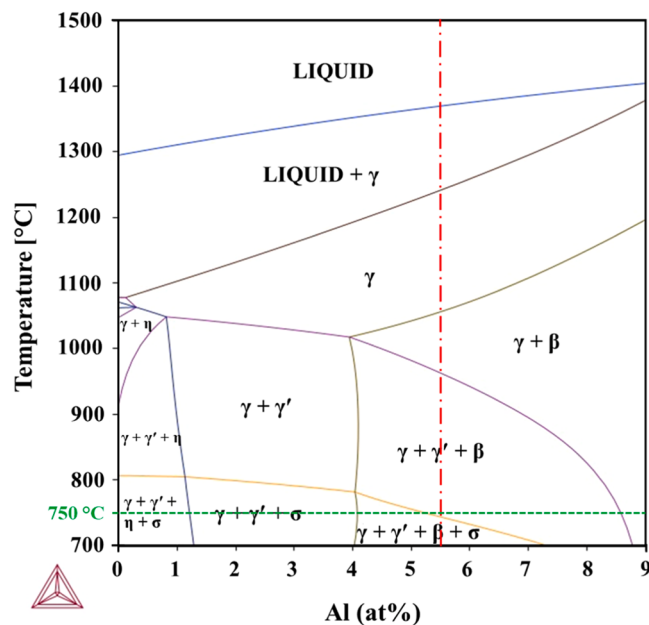


Fig. 1. Phase diagram of $\text{Al}_x\text{Co}_{1.5}\text{CrFeNi}_{1.5}\text{Ti}_y$ (x, y values are in atomic ratio, $x + y = 0.5$). The crystal structure of phases γ , γ' and β correspondingly are A1, L1₂ and B2 in Strukturbericht designation. The proposed alloy contains Al = 5.5 at.% marked by red dashed line, aged at 750 °C marked by green dashed line.

single phase γ (FCC) microstructure.

The electron backscatter diffraction (EBSD) analysis confirmed the formation of a single phase, as shown in Fig. 2(b) and (c). The XRD results presented in Fig. 2(c) further confirms the formation of single-phase FCC. Inset in this figure is the FESEM image revealing the single phase solutionized microstructure of the alloy.

3.2. Aging treatment and microstructural study

Fig. 3(a) presents the aging curve of the alloy at 750 °C, revealing that peak aging occurs at 120 h with a corresponding peak-aged hardness of ~ 550 HV. Notably, the peak-aged alloy exhibits a remarkable ~ 214 % increase in hardness compared to the solutionized state, whose hardness is ~ 175 HV. Hardness values observed below peak aging point are indicative of an underaged state, whereas values exceeding the peak aging point signify an overaged condition. Fig. 3(b) to 3 (f) showcases the formation of two distinct types of precipitates in the alloy during aging: needle-shaped and spherical. In Fig. 3(b), the under-aged microstructure at 24 h of aging displays fine $\text{Ni}_3(\text{Al}, \text{Ti})$ type L1₂ (γ') nanoprecipitates and NiAl-B2 (β) precipitates (as confirmed through TEM discussed in the next paragraph), which are also established as equilibrium phases in the phase diagram (refer Fig. 1). An over-aged microstructure (Fig. 3(c)) taken at 400 h of aging demonstrates the formation of larger γ' precipitates and the occurrence of cellular precipitates at grain boundaries. Cellular precipitates typically emerge during grain growth in alloys. Initially at lower aging times, γ' impedes grain boundary migration. However, during over aging, grain growth starts to get more significant. γ' cannot provide enough strength to hinder grain boundary migration and hence get elongated by the moving

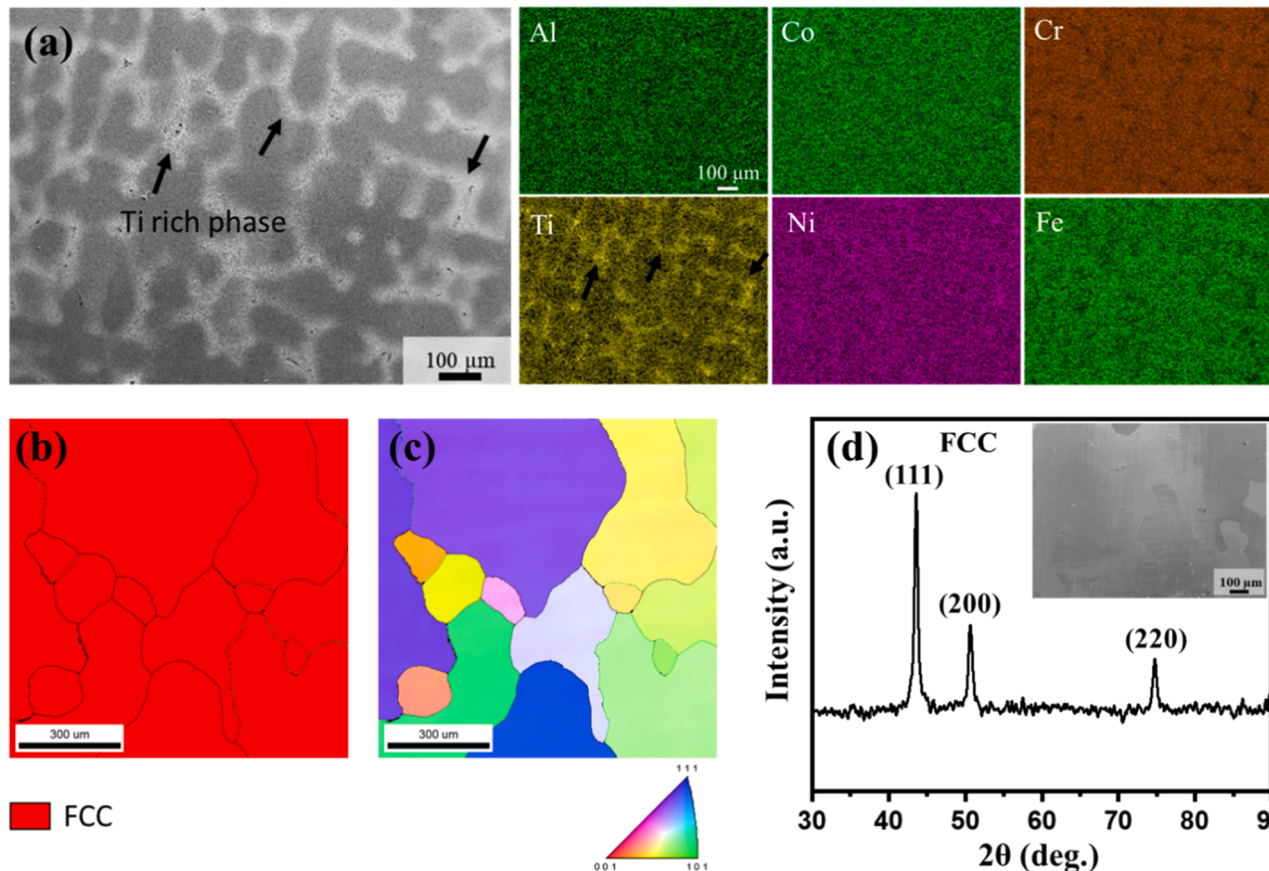


Fig. 2. (a) SEM image of as-cast microstructure with corresponding EDS elemental mapping (scale bar of all elements in EDS mapping is same as shown for Al); (b) phase map, and (c) IPF image from EBSD showing single phase γ grains; (d) XRD diffraction pattern of the solutionized alloy with an inset featuring the FESEM image revealing the microstructure of the alloy.

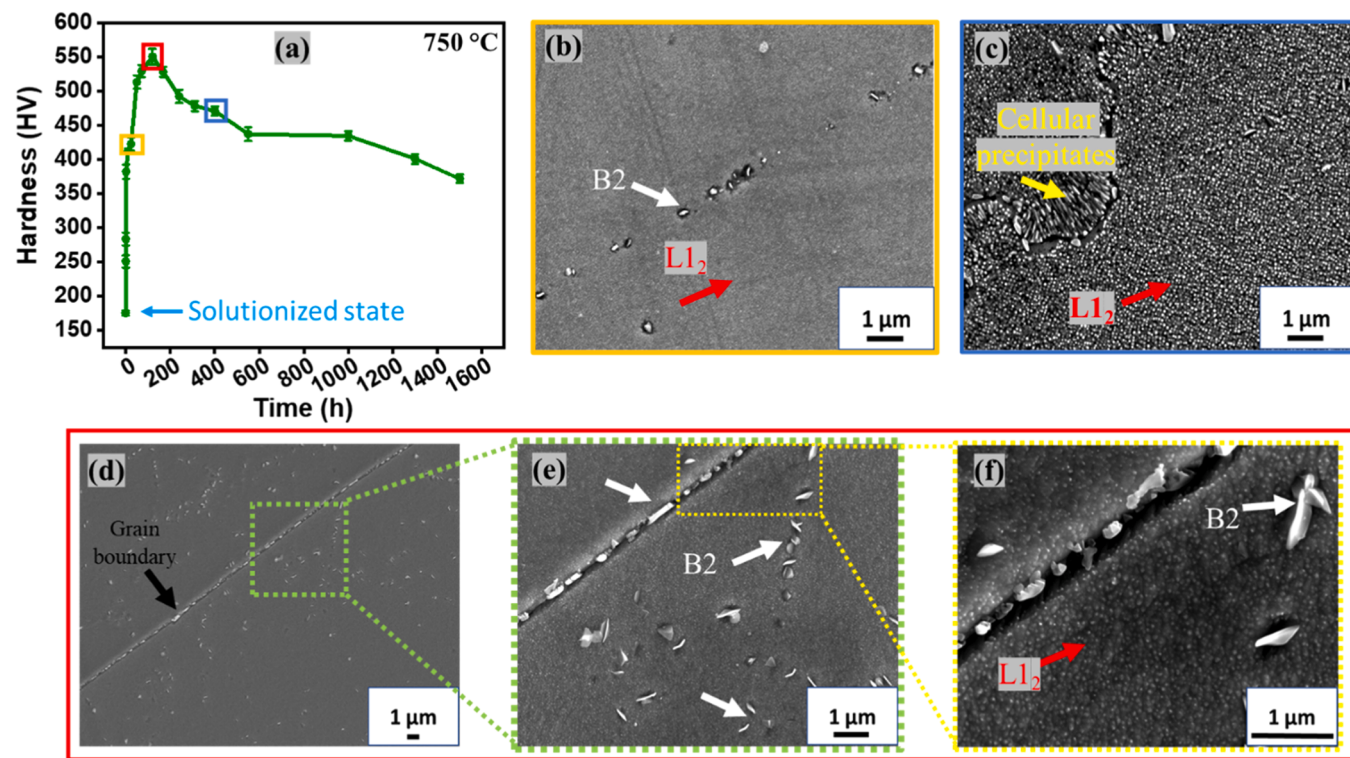


Fig. 3. (a) Aging curve of Al0.3Ti0.2 at 750 °C for various times from 0 h to 1500 h showing peak hardness at 120 h, marked with the red box. Yellow and blue boxes indicate underaged (24 h) and overaged (400 h) conditions, respectively; SEM images of (b) under-aged microstructure at 24 h of aging, (c) over-aged microstructure showing cellular precipitates along with L1₂ at 400 h, (d)-(f) peak aged microstructure showing B2 and L1₂ precipitates. Arrows in (b)-(f) indicate precipitates, white - B2, red - L1₂, and yellow – cellular precipitates.

grain boundaries [28,29]. These cellular precipitates are known to have detrimental effects on the mechanical properties of the alloy [28,29]. Previous studies have also reported the presence of cellular precipitates in CoCrFeNi high entropy alloys with Ti additions [28–30]. SEM images in Fig. 3 (d-f) capture the peak-aged condition, showing the presence of fine L1₂ (γ') precipitates and B2 precipitates. The size of the L1₂ precipitates in the peak-aged condition is approximately 40 nm, while the larger axis of the B2 precipitates measures around 800 nm, confirmed using both SEM and the subsequent TEM analysis. The B2 precipitates exhibit heterogeneous distribution, with a higher concentration at grain boundaries, while the γ' precipitates are homogeneously dispersed within the grains throughout the alloy. σ phase is not observed in solutionized or aged conditions because of high cooling rates that are employed during quenching which suppresses the formation of σ phase [31].

Fig. 4 presents TEM images of the peak-aged sample. The selected area electron diffraction (SAED) pattern in Fig. 4(a) exhibits typical face-centered cubic (FCC) spots with superlattice spots, confirming the presence of the L1₂ phase. The dark field image, captured in Fig. 4(b) by trapping the superlattice spot marked by the red circle in Fig. 4(a), highlights the L1₂ precipitates. Bright-field STEM with EDS analysis in Fig. 4(c) confirms the presence of nano-sized particles rich in Ni, Ti, and Al which are identified as Ni₃(Al, Ti) type γ' precipitates. The misfit between γ' and γ described as $\delta = 2(a_{\gamma'} - a_{\gamma})/(a_{\gamma'} + a_{\gamma})$ is calculated to be -0.75% , where $a_{\gamma'}$ and a_{γ} are the lattice parameters of precipitate and matrix, respectively. The volume fraction of γ' precipitates is ~ 0.55 . Fig. 4(d) displays the bright field image taken in zone axis $Z = [011]_{B2}$ indicating the presence of NiAl B2 precipitate within the microstructure. This observation is further supported by the corresponding SAED pattern shown in Fig. 4(e). In a slightly different composition of Al_{0.2}Co_{1.5}CrFeNi_{1.5}Ti_{0.3} (in atomic ratio), it is noteworthy that the Heusler type L2₁ phase has been found instead of B2 [32,33]. This deviation can be attributed to the higher Ti content in this alloy compared

to the alloy under primary investigation. It has been observed that the introduction of Ti tends to stabilize the L2₁ phase in high entropy alloys [34]. The L2₁ structure shares similarities with the B2 structure, both being ordered BCC structures. While SAED pattern from the Fig. 4(e) confirms the presence of the B2 phase, no conclusive evidence has been found to confirm the presence of the L2₁ phase in the Al0.3Ti02 alloy. Nevertheless, the possibility of L2₁ precipitates in this alloy cannot be entirely ruled out.

For further studies, the focus has been restricted to solutionized and peak aged conditions in order to elucidate the influence of precipitates on hardening mechanisms, leading to increased hardness and strength.

3.3. Tensile behavior

Fig. 5(a) and (b) show the engineering and true stress-strain curves, respectively, obtained from uniaxial tension tests conducted at room temperature for the solutionized and peak-aged Al0.3Ti02 HEA. Table 1 provides the corresponding yield strength (σ_y), ultimate tensile strength (σ_{UTS}) and strain to fracture (ϵ_f) values for both sample conditions. The results indicate that peak aging leads to a substantial increase in yield strength and ultimate strength by approximately 175 % and 75 %, respectively, while still maintaining a reasonable strain to fracture of $\sim 14\%$ as against the solutionized sample. Fig. 5(c) illustrates the work-hardening curves for the solutionized and peak-aged samples. It is evident that the work-hardening behavior is significantly enhanced in the peak-aged sample compared to the solutionized one. The solutionized alloy exhibits a three-stage work-hardening behavior. Initially, there is a rapid decrease in hardening, indicating a softening effect. This can be attributed to processes such as stable dislocation generation and easy glide of dislocations. In the second stage, there is a gradual increase in hardening, suggesting the activation of additional strengthening mechanisms which increase the resistance to deformation. Finally, in the third stage, the work hardening decreases again to

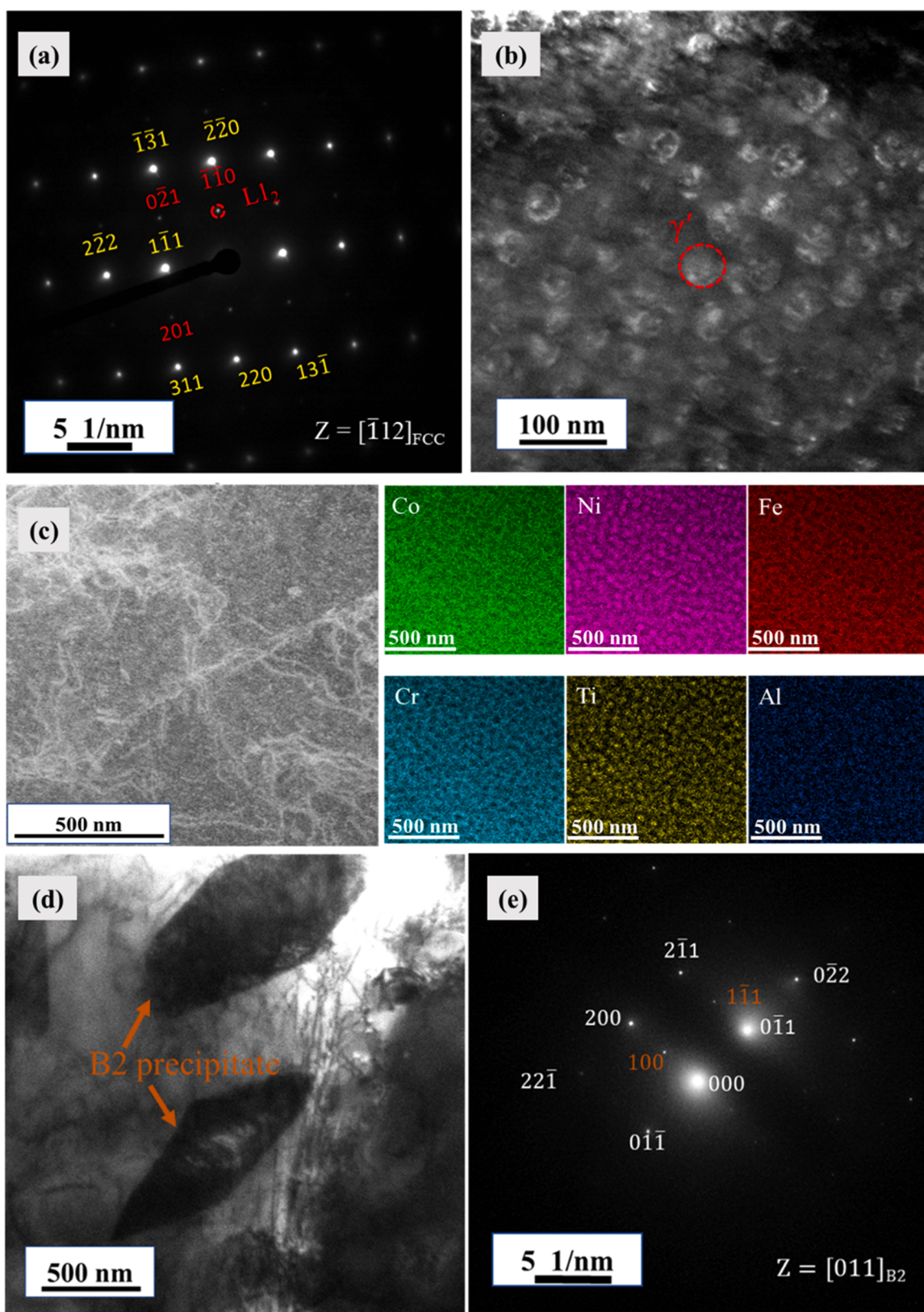


Fig. 4. TEM analysis of peak aged condition sample showing: (a) SAD pattern taken in $Z = [\bar{1}12]_{\text{FCC}}$ confirming γ (FCC); (b) dark field image from the superlattice spot encircled in red in (a). The dashed circle in red in (b) indicates a γ' ($\text{L}1_2$) precipitate; (c) TEM-EDS confirming the presence of $[\text{Ni}_3(\text{Al}, \text{Ti})]$ type $\text{L}1_2$ precipitates; (d) bright field image showing B2 precipitates present in the microstructure, (e) corresponding SAD pattern, $Z = [011]_{\text{B}2}$.

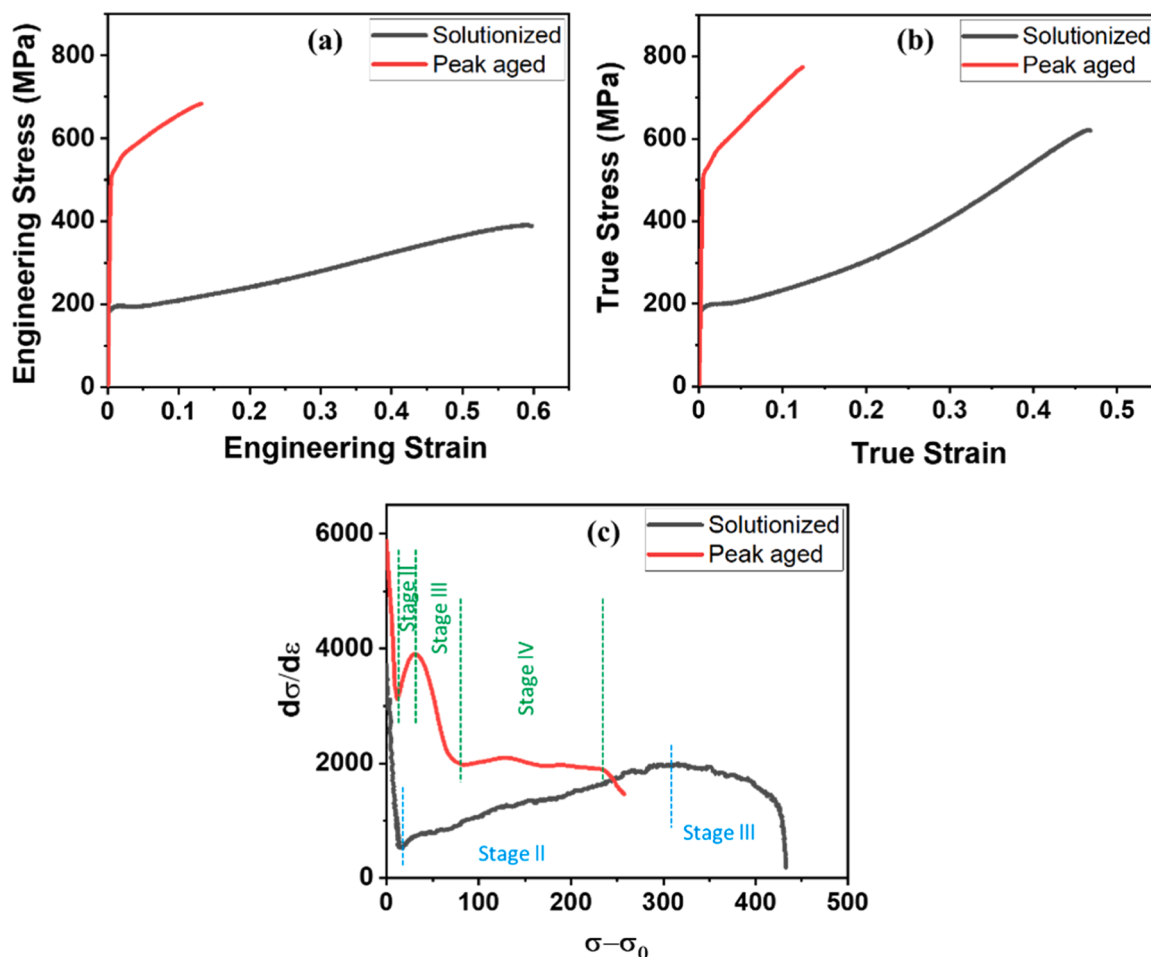


Fig. 5. (a) Engineering stress-strain, (b) True stress-strain plots for solutionized and peak aged condition of Al0.3Ti02 and (c) corresponding strain hardening plots.

Table 1

Mechanical properties of solutionized and peak aged Al0.3Ti02 HEA samples upon tensile testing.

Al0.3Ti02 Sample Condition	σ_y (MPa)	σ_{UTS} (MPa)	ε_f
Solutionized	185 ± 10	391 ± 6	60 ± 6
Peak aged	510 ± 5	685 ± 5	14 ± 5

fracture. This decline in hardening can be realised by the dominance of dynamic recovery over hardening. In contrast, the peak-aged alloy displays a more complex work-hardening behavior. Initially, there is a sharp decrease in hardening, followed by a steep increase and then a gradual decrease in work hardening towards failure. The distinct work-hardening behavior observed in the two conditions are closely related to the activated deformation mechanisms within the samples. A comprehensive explanation of these mechanisms will be provided in the subsequent discussion section of the paper.

Fig. 6 presents SEM images of the fractographic analysis. In Fig. 6(a),

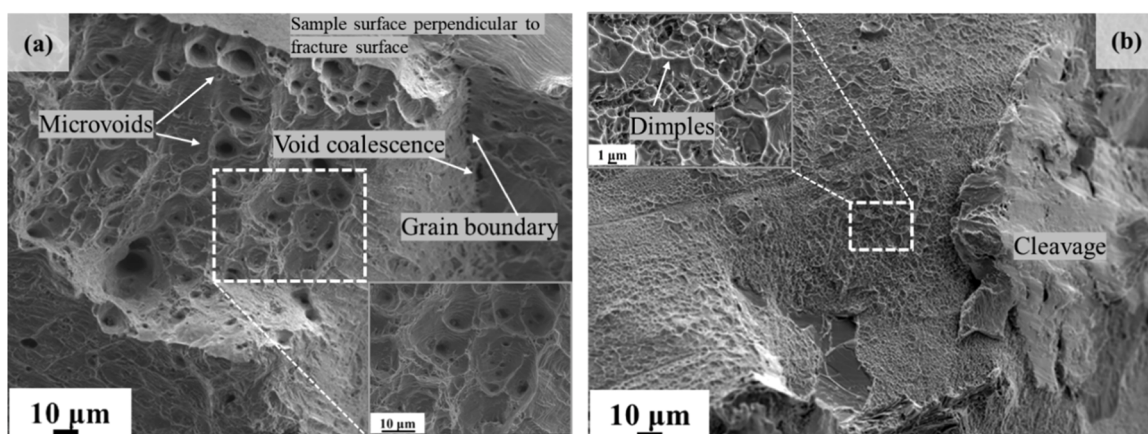


Fig. 6. SEM micrographs showing tensile fracture surface of (a) solutionized and (b) peak aged Al0.3Ti02 HEA.

corresponding to the solutionized condition, the presence of micro-voids with a size of $\sim 10 \mu\text{m}$ indicates a ductile fracture mode. This is consistent with the ductility observed in tensile testing. The fracture appears to be intergranular, as the entire grains are observed to have been pulled apart. Micro-void coalescence is observed to occur along the grain boundaries within the material.

This plays a pivotal role in the subsequent crack formation and eventual failure of the specimen. On the other hand, Fig. 6(b) represents the peak-aged condition, where a combination of micro-scale dimples of $\sim 1 \mu\text{m}$ and cleavage-type features are observed. This suggests a mixed-mode fracture behavior. The micrograph further indicates that the fracture predominantly occurs within the grains, indicating a trans-granular fracture mode. The insets in Fig. 6(a) and (b) provide fractographic information at higher magnifications for better observation and understanding.

4. Discussion

4.1. Aging behavior

The aging curve depicted in Fig. 3(a) exhibits an initial rapid increase in hardness with increasing aging time, reaching its peak at 120 h. This observation suggests the alloy undergoes a relatively fast aging process, indicating accelerated kinetics. The microstructural analysis confirms the presence of two distinct types of precipitates, namely the B2 (β) and L1₂ (γ') phases (Figs. 3 and 4), in the peak aged condition, which aligns with the phase diagram predictions (Fig. 1). Following the peak aging stage, the hardness of the alloy exhibits a noticeable decrease. This decline can be attributed to the coarsening of precipitates and the formation of cellular precipitates, as illustrated in Fig. 3(c), which can have a detrimental effect on the mechanical properties of the material [28, 29]. As the aging time progresses, the γ' precipitates undergo dissolution and subsequent reprecipitation, resulting in a morphological transformation from spherical to cellular (η) precipitates [27, 28]. The formation of cellular precipitates significantly impacts the material's properties, leading to a decline in hardness. Fig. 7 provides a comparative analysis of age hardening behavior of Al03Ti02 alloy with other non-equiautomatic CoCrFeNi high entropy alloys reported in the literature, all aged at the same temperature [10]. Notably, the peak aging time for Al03Ti02 alloy is 120 h, which differs from the 240 h reported for other alloys. The decreased peak aging time for the currently studied alloy can be a result of alloy composition and precipitate types. Al03Ti02 having more Al content, which diffuses easily than Ti, leads to shorter peak aging time as compared to Al02Ti03 and Ti05 ($\text{Al}_{0.2}\text{Co}_{1.5}\text{CrFeNi}_{1.5}\text{Ti}_{0.3}$ and $\text{Co}_{1.5}\text{CrFeNi}_{1.5}\text{Ti}_{0.5}$ in atomic ratio, respectively). Faster kinetics

than Al05 ($\text{Al}_{0.5}\text{Co}_{1.5}\text{CrFeNi}_{1.5}$ in atomic ratio) is due to the higher density of coherent and nano sized L1₂ precipitates formed in the considered alloy (Fig. 3), which nucleate and grow faster than in-coherent B2 precipitates in Al05 alloy [25]. Furthermore, the increment in hardness from the solutionized to peak aged condition is found to be the highest for Al03Ti02 alloy ($\sim 214\%$) compared to the other alloys studied previously. This can be attributed to the presence of two distinct types of precipitates in Al03Ti02 alloy, which contribute to its hardness. Presence of numerous L1₂ effectively impedes the dislocation motion leading to increase in hardness. Though B2 precipitates are fewer in number and present mostly at the grain boundaries, they overall increase the hardness because of introducing larger lattice strains into the system and have generally a stronger hardening effect than L1₂ [35]. In contrast, other alloys typically exhibit only one type of precipitation in the peak-aged condition. The phase diagram presented in Fig. 1 confirms the thermodynamic stability of both B2 and L1₂ precipitates at 750 °C, supporting the current observations.

The difference in hardness between Al03Ti02 alloy and other previously studied alloys in the solutionized condition can be attributed to the concentration of Ti. The higher the amount of Ti in the alloy, the higher the hardness. This can be explained by the larger atomic radius of Ti compared to the other elements present in these alloys. The presence of Ti with a larger atomic radius induces greater distortion in the crystal lattice, resulting in increased hardness. Therefore, Al03Ti02 alloy exhibits higher hardness than Al05 alloy due to its higher Ti concentration. However, its hardness is lower than that of Ti05 and Al02Ti03 alloy in the solutionized condition, which contains an even higher concentration of Ti and thus experiencing greater distortion and subsequent hardness.

It is observed that B2 is formed heterogeneously in the system while L1₂ is homogeneously distributed (Fig. 3 (d-f)). This distinction is attributed to the differences in the energy barriers for their formation within the FCC matrix [25]. The coherent-ordered FCC L1₂ phase has a relatively low energy barrier, facilitating its homogeneous distribution throughout the matrix. On the other hand, the formation of the ordered BCC B2 phase within the FCC matrix requires higher energy, making it more likely to form at grain boundaries and sites with high energy, such as heterogeneities or voids. The B2 precipitates adopt a needle-like morphology, which helps to minimize the lattice misfit strain between the FCC (γ) matrix and the B2 precipitates. In contrast, the L1₂ precipitates exhibit a spherical shape due to their near-zero lattice misfit strain with the matrix. This low lattice misfit allows for a more favourable arrangement of atoms, resulting in a spherical morphology.

4.2. Work hardening behavior

4.2.1. Solution-treated

To investigate the strain hardening behavior of Al03Ti02 HEA, TEM samples were taken from the near fracture regions for both conditions after failure under tensile loading. The solutionized alloy displays a distinct three-stage hardening behavior, as depicted in Fig. 5(c). The initial decrease in hardening is a characteristic feature observed in low SFE FCC materials [16]. This behavior arises from the predominance of single slip and stable dislocation generation [16, 36]. Considering that most CoCrFeNi high entropy alloys possess low SFE values, it is reasonable to expect a low stacking fault energy for the present alloy as well. Previous studies have reported SFE values of 20 mJ/m² for CoCrFeNi [37], 73 mJ/m² for Al_{0.57}CoCrFeNi [38], and 25–50 mJ/m² for (CoCrFeMnNi)₉₆(TiAl)₄ alloy [39].

In the second stage of strain hardening of solutionized Al03Ti02 alloy, there is a gradual increase in the hardening response. This behavior can be attributed to the interaction between dislocations, stacking faults, and the formation of LC locks. Bright-field TEM image in Fig. 8(a) shows a high density of stacking faults in the FCC matrix. A magnified image is shown in Fig. 8(b) revealing the intersection of stacking faults. The inset in this figure shows the fast Fourier transformation (FFT) image with crossing diffraction fringes marked by

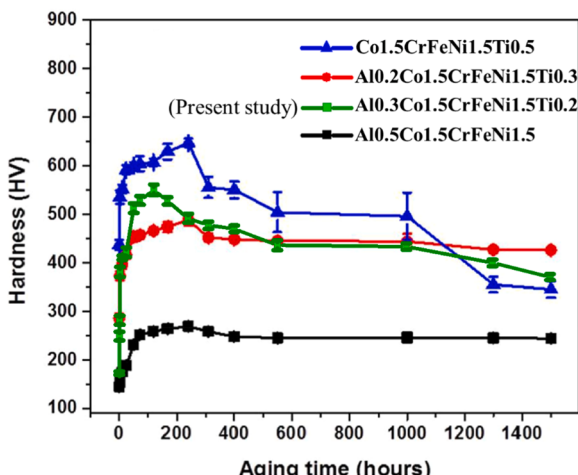


Fig. 7. Aging behavior of different CoCrFeNi based HEAs containing varying additions of Al and Ti at 750 °C [10].

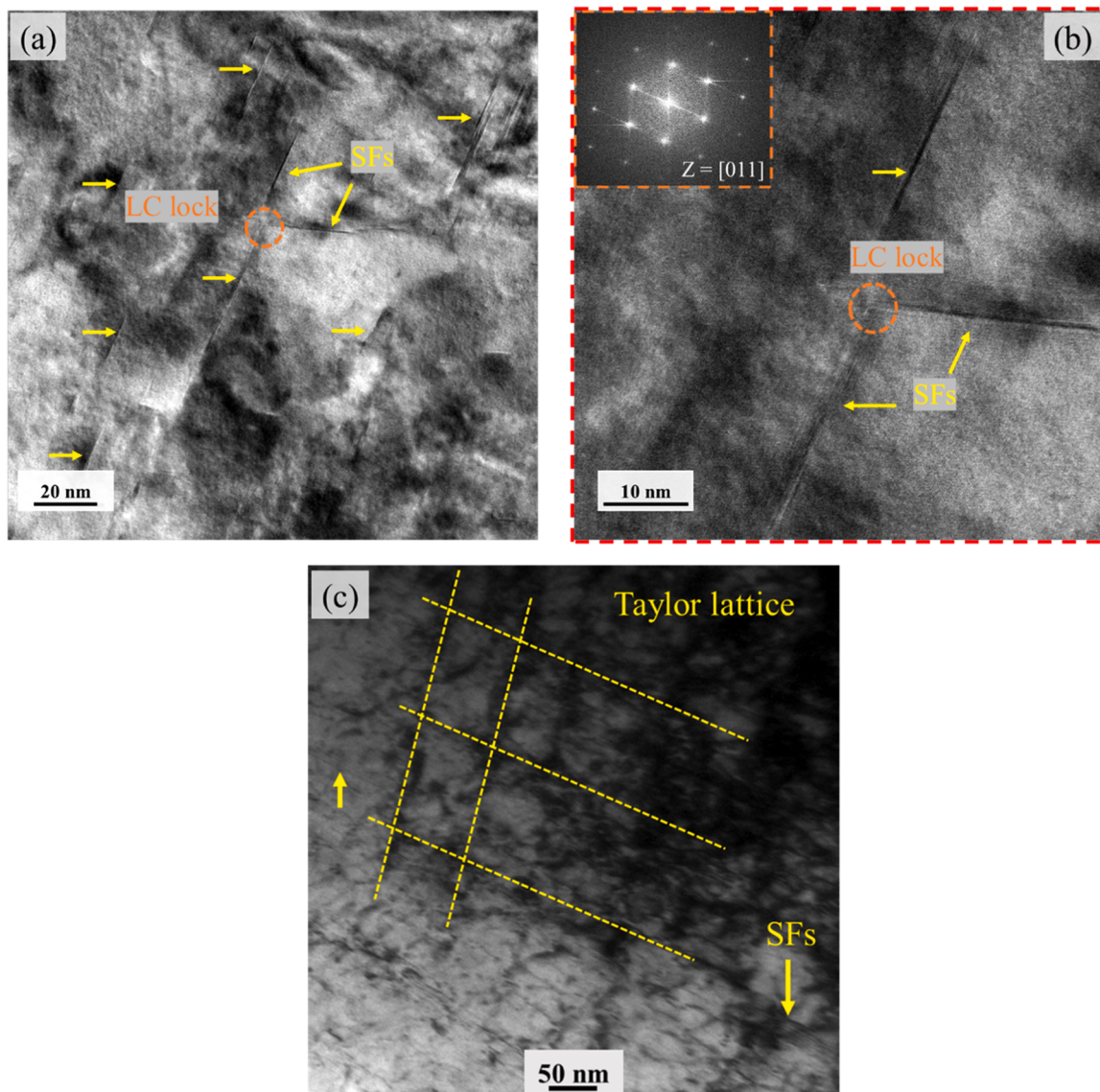


Fig. 8. TEM images of solutionized Al_{0.3}Ti_{0.2} HEA tensile tested to fracture: (a) bright field (BF) image showing the presence of numerous stacking faults (marked with yellow arrows) and LC lock; (b) Magnified image taken from the region marked by red dashed box in (a) showing intersection of stacking faults. The inset shows FFT image with crossing diffraction fringes marked by arrows confirming the presence of stacking faults (SFs) instead of twinning; (c) bright field image showing dislocation substructures, i.e., Taylor lattice and stacking faults.

arrows confirming the presence of intersecting stacking faults (SFs) instead of twinning. It should be noted that twinning was not observed in the alloy. The presence of stacking faults and the absence of twinning suggest that the SFE of the material is sufficiently low to allow for the formation of stacking faults but not low enough to initiate twinning. It is widely recognized that deformation-induced twinning serves as a significant mechanism for deformation in FCC metals characterized by SFEs lower than $\sim 25 \text{ mJ/m}^2$ [40]. An increase in strain hardening due to formation of SFs has also been observed in Al_{0.1}CoCrFeNi HEA [41]. Some SFs intersect with each other to form LC locks (Fig. 8(a), (b)), as was also reported elsewhere [15,42–44]. The formation of LC locks is a gradual process that necessitates strain accumulation to activate different primary slip systems [45]. This phenomenon contributes to the hardening observed at higher strain levels in the material. The formation of the LC lock requires splitting of a perfect dislocation with a Burgers vector of $\frac{a}{2}\langle 110 \rangle$ into two Shockley partial dislocations with Burgers vectors of $\frac{a}{6}\langle 112 \rangle$. This process leads to the introduction of SFs within the crystal lattice. The interaction between the leading partial dislocations results in the formation of stable stair-rod dislocations that remain

immobile, forming the characteristic LC locks [45]. It is well established that LC locks play a crucial role in the strengthening mechanism of FCC metals through strain hardening. Because of their sessile nature, LC locks can operate as powerful barriers to dislocation motion, inhibiting dislocation glide and contributing to material strengthening. Additionally, LC locks can serve as Frank-Reed sources for dislocation multiplication, further contributing to work hardening [46]. Further, it can be seen in the bright field TEM image in Fig. 8(c) that Taylor lattice type substructures are formed in solutionized alloy. This substructure also contributes to the hardening as it impedes dislocation motion like a refined grain structure obstructs dislocation motion [47]. Low SFE, high lattice friction, and planar glide are the factors that promote the formation of Taylor lattices [47,48]. The presence of Al and Ti atoms in the present alloy leads to an increase in friction stress due to their larger atomic radii compared to other elements, favouring the formation of a Taylor lattice structure.

With further plastic deformation, the curve transitions into region 3, where the strain hardening rate decreases incessantly until fracture as the strain hardening mechanisms associated with SFs, LC locks and

Taylor lattices get saturated and dynamic recovery takes over hardening.

4.2.2. Peak-aged

Peak-aged Al03Ti02 exhibits complex strain-hardening behavior, as depicted in Fig. 5(c). The initial decrease is attributed to the easy glide of dislocations [36]. The slope of this initial decline in hardening for aged condition is similar to the stage I of solutionized condition (Fig. 5(c)), suggesting that initial movement and glide of dislocations in the aged alloy is confined to the FCC matrix. After further deformation in the solutionized alloy, numerous SFs and LC locks cause a gradual increase in hardening. The hardening is more prominent towards higher strain levels as activation of multiple slip systems is required to form LC locks, as discussed earlier. On the other hand, in peak aged alloy, before such hardening begins to operate, the presence of ordered L1₂ domains, present densely and homogeneously throughout the matrix, obstruct the movement of dislocations leading to an early increase in hardening compared to the solutionized alloy.

Fig. 9(a) demonstrates a significant number of paired dislocations in the peak-aged condition. These coupled dislocations are similar to those observed in γ' strengthened Ni superalloys post deformation [21,22]. Dislocations tend to dissociate into partials when the slip is halted by the ordered precipitates, as this is energetically favorable for the system [49]. In the FCC matrix, full dislocations have a Burgers vector of $\frac{a}{2}\langle 110 \rangle$ whereas in the ordered L1₂ domains, they have a Burger vector of $a\langle 110 \rangle$. As a result, slip of a full FCC matrix dislocation through the L1₂ precipitates will lead to the formation of anti-phase boundaries, which are undesirable configurations of high energy. Consequently, when the second $\frac{a}{2}\langle 110 \rangle$ full FCC matrix dislocation propagates through the material, it effectively restores the crystal structure within the regions containing the ordered precipitates. This interaction between dislocations and the L1₂ precipitates leads to an increase in strain-hardening, as illustrated by region II of aged alloy in Fig. 5(c).

Fig. 9(b) shows that Orowan loops coexist with partial dislocations. Orowan loops are formed because of the dislocation bypass mechanism. Precipitates, which are not sheared, confine the dislocations within the FCC matrix. The dislocations bow around the precipitates leaving behind loops. The co-existence of Orowan loops and partial dislocations has been observed before in nickel-based superalloy GH4037 [50]. Formation of these loops also leads to the strengthening of the aged Al03Ti02 alloy.

Stress estimations due to different strengthening mechanisms are made. The precipitate shearing stress (σ_{sh}), associated with a full dislocation cutting through a L1₂ precipitate [44,51], critical resolved shear stress (CRSS) (σ_c) for the paired dislocations to cut through the L1₂ precipitates [50] and the Orowan dislocation looping stress (σ_{or}) [50, 51] are obtained as follows:

$$\sigma_{sh} = 0.81M \frac{\gamma_{APB}}{2b} \left(\frac{3\pi f}{8} \right)^{1/2} \quad (1)$$

$$\sigma_c = \frac{Gb}{2\pi l} (2\alpha) \left(\frac{2\pi \gamma_{APB}}{\alpha Gb^2} - 1 \right)^{1/2} \quad (2)$$

$$\sigma_{or} = \frac{Gb}{2\pi l} \ln \left(\frac{l}{r_0} \right) \quad (3)$$

where M is the Taylor factor and is equal to 3.06 for polycrystalline FCC matrix, $\gamma_{APB} = 0.20 J m^{-2}$ is the anti-phase boundary energy for Ni₃(Al, Ti) precipitates in Ni superalloys [52], b is the Burgers vector of γ matrix (~ 0.2626 nm), f is the volume fraction of precipitates (around 0.55), $l \sim 40$ nm is the average edge to edge inter-precipitate distance, $\alpha = 1$ and dimensionless constant which explains the elastic repulsion between the coupled dislocations [50], $G = 77$ GPa is the shear modulus of Ni₃(Al, Ti) precipitates [50], r is the average size of precipitates (~ 40 nm), r_0 is dislocation core radius $\approx b$.

As per the calculations, the strengthening contributions from σ_{sh} , σ_c and σ_{or} are about 760 MPa, 470 MPa, and 400 MPa, respectively. Since σ_{sh} is higher as compared to other two, it is safe to say that shearing by full dislocations does not take place. The stress values, σ_c and σ_{or} , are close to each other. Also, it has been reported previously that the critical size of L1₂ precipitates in HEAs to change the strengthening mechanism from shearing to Orowan looping is ~ 45 nm [53], which is comparable to the size of γ' precipitates in the considered peak aged alloy (~ 40 nm). These factors support the coexistence of Orowan loops and partial dislocations, as observed in Fig. 9(b).

Post the increase in hardening due to precipitate strengthening, there is a steep decrease, as seen in region III in Fig. 5(c). Fig. 9(c) presents the high-resolution transmission electron microscopy (HRTEM) image of the peak aged Al03Ti02 after strained to fracture. The FFT analysis in Fig. 9(d) does not indicate superlattice spots from the L1₂ phase, which implies that the destruction of the L1₂ order has occurred. The L1₂ ordered particles will be totally sheared through once several partial dislocations pass through these domains. Consequently, these domains will offer far less resistance to the subsequent dislocations; hence, the movement of paired dislocations is not needed for further slip. Consecutive slip of paired dislocations on the same slip plane causes a decrease in hardening.

The increment in yield strength from solutionized to the aged condition is 346 MPa which is closer to σ_c and σ_{or} than σ_{sh} . Therefore, we can say that shearing by full dislocations is not favourable. Further, since the density of partial dislocations is more as compared to Orowan loops and the ordered structure has been destroyed, as seen if Fig. 9(c) and (d) implies that precipitate shearing by partial dislocations is the main mechanism of strengthening in the studied HEA.

Following the sharp decline in region III, the peak aged alloy exhibits a gradual decrease in hardening observed in region IV of Fig. 5(c). This behavior suggests that strengthening mechanisms are actively countering the recovery processes. Examination of the microstructure in Fig. 9(f) reveals several key features, including high-density dislocation walls (HDDWs), stacking faults, and LC locks. The elimination of ordered domains within the material allows for the emergence of these dislocation substructures. These dislocation substructures play a crucial role in augmenting the overall strengthening response of the alloy by impeding dislocation motion and delaying necking. HDDWs have been observed previously [16,44] and are formed when there is a high accumulation of dislocations in localized regions within the material. Further, an inverse fast Fourier transform (IFFT) was performed using the $(11\bar{1})$ spatial frequencies of the region shown in Fig. 9(c). The resulting IFFT image is displayed in Fig. 9(e) and provides evidence of SFs and numerous dislocations within the deformed peak-aged sample. Subsequent to region IV, strengthening factors saturate and reach their limits leading to the decline of work to fracture. The main deformation mechanism of solutionized and peak-aged alloys is planar slip of dislocations, and twinning is not observed. Fig. 9(g) illustrates the planar slip of dislocations along $\{111\}$ primary slip planes. In metallic materials, dislocation slip can take on either a planar or wavy character. Planar slip is facilitated by three factors: high lattice friction, low SFE, and the presence of ordered domains [44,54,55]. The Al03Ti02 alloy is expected to have high lattice friction due to the presence of Al and Ti atoms, as well as low SFE and the presence of ordered domains in the peak aged state. Therefore, deformation by planar slip is likely to occur in this alloy. Also, it has been observed in most of the FCC HEAs that deformation takes place by planar slip [44,54].

B2 precipitates present in the peak-aged alloy also contribute to the overall strengthening of the alloy. These micro precipitates act as obstacles for the movement of dislocations leading to the formation of dislocation forests around these precipitates [56]. As discussed earlier, B2 precipitates are mostly formed at grain boundaries. Hence stress concentration around these precipitates at the grain boundaries leads to loss of ductility [44,57]. Nonetheless, these precipitates augment the

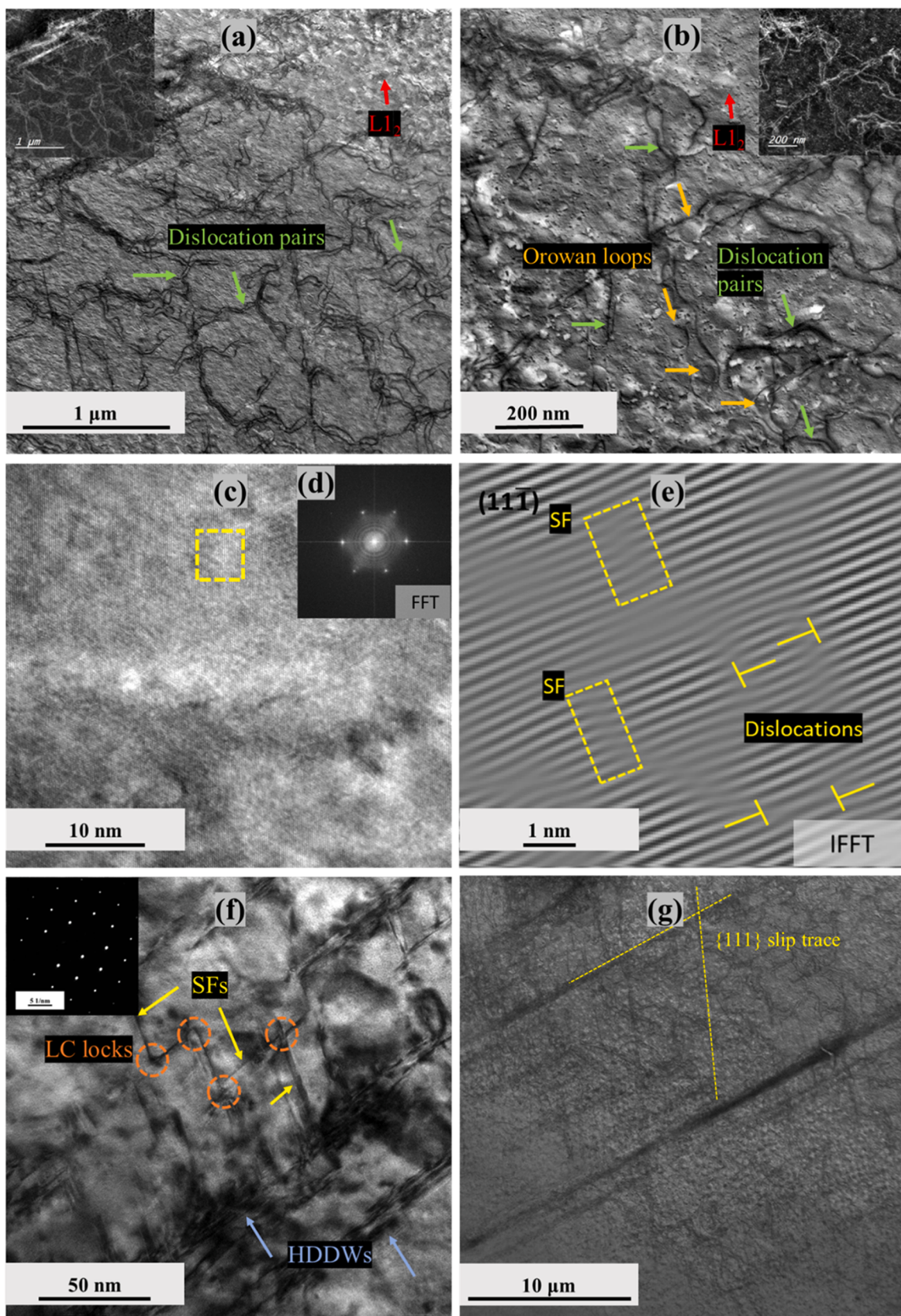


Fig. 9. TEM images taken along $z = [011]$ of the aged Al_{0.3}Ti_{0.2} alloy tensile tested to fracture: (a) and (b) STEM-BF images and their corresponding HAADF images in the insets. (a) shows a high density of dislocation pairs and L₁₂ precipitates, (b) Orowan looping is seen around L₁₂ precipitates which coexist with the dislocation pairs; (c) HRTEM image showing the absence of ordered L₁₂ phase, which is confirmed by the (d) FFT given in the inset; (e) IFFT of marked region in (c) showing the presence of SFs and numerous dislocations; (f) BF image showing the presence of SFs marked with arrows, LC locks and high-density dislocation walls (HDDWs). SADP in the inset confirms the presence of SFs and no twinning; (g) STEM-BF image revealing the {111} slip traces intersecting at $\sim 70^\circ$

alloy's overall strength and hardness. For B2 phase, stress contribution to yield strength increment by the Orowan dislocation bypassing is given by the equation below [58].

$$\sigma = M \cdot \frac{0.4Gb}{\pi\sqrt{1-\nu}} \cdot \frac{\ln(2\bar{r}/b)}{\lambda_p} \quad (4)$$

where M is the Taylor factor and is equal to 3.06 for polycrystalline FCC matrix, $G = 80$ GPa is the shear modulus for FeCoCrNiMn HEA [59], b is the Burgers vector of γ matrix (~ 0.2626 nm), $\nu = 0.265$ is Poisson ratio for FeCoCrNiMn HEA [59], $\bar{r} = \sqrt{\frac{2}{3}} r$ and r is mean radius of precipitates (~ 290 nm). λ_p is the average edge to edge inter-precipitate distance and is equal to $2\bar{r} \left(\sqrt{\frac{\pi}{4f}} - 1 \right)$ where f is the volume fraction of B2 precipitates (~ 0.0045).

Contribution of B2 precipitates towards yield strength by Orowan dislocation and bowing mechanism is ~ 12 MPa which is far less than the strength contribution by L1₂ precipitates.

5. Conclusions

In this work, the Al03Ti02 alloy was subjected to solutionizing and aging treatments to understand the role of alloying and precipitation on the mechanical response. It was found that the hardness of the alloy increased significantly, by $\sim 214\%$, from the solutionized to the peak aged condition. Microstructural analysis using SEM and TEM confirmed the presence of macro-sized B2 precipitates and nano sized L1₂ precipitates.

Tensile tests were conducted for both the solutionized and peak-aged conditions. The increment in yield strength of the alloy with aging is $\sim 187\%$. Fractography after tensile tests revealed ductile fracture in case of solutionized alloy while as mixed mode type of fracture for peak aged alloy. The hardening behavior of the two conditions exhibited notable differences. In the solutionized condition, where only the FCC phase is present, strain hardening was primarily attributed to the formation of SFs, LC locks, and the development of a Taylor lattice. In the peak aged condition, strengthening was mostly due to γ' precipitates. TEM images indicated a large number of paired dislocations, formed due to inhibition of slip by the ordered γ' precipitates, coexist with the Orowan loops. Stress calculations were also performed that supported the TEM observations. The main strengthening mechanism in this condition was associated with the shearing of L1₂ precipitates by partial dislocations, while additional hardening was observed due to the interaction of stacking faults and formation of LC locks after the ordering by γ' precipitates is destroyed by partial dislocations. It was found that strength contribution by B2 precipitates is far less than the L1₂ precipitates present in the alloy at the peak aged condition. Deformation mainly occurs by planar slip along the {111} primary slip planes. These findings highlight the significant role of precipitates, dislocation substructures, and microstructural evolution in the mechanical response and strengthening mechanisms of the Al03Ti02 alloy.

Declaration of competing interest

The authors declare that they have no known competing financial interests or personal relationships that could have appeared to influence the work reported in this paper.

Acknowledgment

JJ and SN would like to acknowledge Science and Engineering Research Board of Department of Science and Technology (SERB-DST) for providing financial support through CRG grant (File no.: CRG/2020/000955). Authors also like to thank the support received from Department of Materials Science and Engineering and Central Research

Facilities (CRF) such as FESEM-EBSD, EDS and TEM at IIT Delhi; and the Department of Metallurgical and Materials Engineering, IIT Roorkee for providing HRTEM facilities. EWH appreciates the National Science and Technology Council (NSTC), Taiwan, for financial support through Grant No. NSTC 112-2811-E-A49-521, NSTC 112-2224-E-007-003 and NSTC 112-2221-E-A49-027. EWH sincerely thanks the help from the High Entropy Materials Center of the National Tsing Hua University from The Featured Areas Research Center Program within the framework of the Higher Education Sprout Project by the Ministry of Education (MOE) in Taiwan for their support.

References

- [1] B. Cantor, Multicomponent high-entropy Cantor alloys, *Prog. Mater. Sci.* 120 (2021) 100754, <https://doi.org/10.1016/j.pmatsci.2020.100754>.
- [2] B. Cantor, I.T.H. Chang, P. Knight, A.J.B. Vincent, Microstructural development in equiatomic multicomponent alloys, *Mater. Sci. Eng. A* 375-377 (2004) 213-218, <https://doi.org/10.1016/j.msea.2003.10.257>.
- [3] K. Biswas, J.W. Yeh, P.P. Bhattacharjee, J.T.M. DeHosson, High entropy alloys: key issues under passionate debate, *Scr. Mater.* 188 (2020) 54-58, <https://doi.org/10.1016/j.scriptamat.2020.07.010>.
- [4] M.H. Tsai, J.W. Yeh, High-entropy alloys: a critical review, *Mater. Res. Lett.* 2 (2014) 107-123, <https://doi.org/10.1080/21663831.2014.912690>.
- [5] J.W. Yeh, Y.L. Chen, S.J. Lin, S.K. Chen, High-entropy alloys - a new era of exploitation, *Mater. Sci. Forum* 560 (2007) 1-9, <https://doi.org/10.4028/www.scientific.net/MSF.560.1>.
- [6] J.W. Yeh, S.K. Chen, S.J. Lin, J.Y. Gan, T.S. Chin, T.T. Shun, C.H. Tsau, S.Y. Chang, Nanostructured high-entropy alloys with multiple principal elements: novel alloy design concepts and outcomes, *Adv. Eng. Mater.* 6 (2004) 299-303, <https://doi.org/10.1002/adem.200300567>.
- [7] E.P. George, D. Raabe, R.O. Ritchie, High-entropy alloys, *Nat. Rev. Mater.* 4 (2019) 515-534, <https://doi.org/10.1038/s41578-019-0121-4>.
- [8] F. He, Z. Wang, Q. Wu, J. Li, J. Wang, C.T. Liu, Phase separation of metastable CoCrFeNi high entropy alloy at intermediate temperatures, *Scr. Mater.* 126 (2017) 15-19, <https://doi.org/10.1016/j.scriptamat.2016.08.008>.
- [9] Y.J. Zhou, Y. Zhang, Y.L. Wang, G.L. Chen, Solid solution alloys of AlCoCrFeNi Ti x with excellent room-temperature mechanical properties, *Appl. Phys. Lett.* 90 (2007), <https://doi.org/10.1063/1.2734517>.
- [10] V. Nandal, R. Sarvesha, S.S. Singh, E.W. Huang, Y.J. Chang, A.C. Yeh, J. Jain, S. Neelakantan, Enhanced age hardening effects in FCC based Co1.5CrFeNi1.5 high entropy alloys with varying Ti and Al contents, *Materialia (Oxf)* 13 (2020) 100823, <https://doi.org/10.1016/j.mtla.2020.100823>.
- [11] Z. Fu, L. Jiang, J.L. Wardini, B.E. MacDonald, H. Wen, W. Xiong, D. Zhang, Y. Zhou, T.J. Rupert, W. Chen, E.J. Lavernia, A high-entropy alloy with hierarchical nanoprecipitates and ultrahigh strength, *Sci. Adv.* 4 (2018) 1-9, <https://doi.org/10.1126/sciadv.aat8712>.
- [12] Y.J. Chang, A.C. Yeh, The evolution of microstructures and high temperature properties of AlxCo1.5CrFeNi1.5Ti y high entropy alloys, *J. Alloys Compd.* 653 (2015) 379-385, <https://doi.org/10.1016/j.jallcom.2015.09.042>.
- [13] X.H. Du, W.P. Li, H.T. Chang, T. Yang, G.S. Duan, B.L. Wu, J.C. Huang, F.R. Chen, C.T. Liu, W.S. Chuang, Y. Lu, M.L. Sui, E.W. Huang, Dual heterogeneous structures lead to ultrahigh strength and uniform ductility in a Co-Cr-Ni medium-entropy alloy, *Nat. Commun.* 11 (2020), <https://doi.org/10.1038/s41467-020-16085-z>.
- [14] T. Yang, Y.L. Zhao, Y. Tong, Z.B. Jiao, J. Wei, J.X. Cai, X.D. Han, D. Chen, A. Hu, J. Kai, K. Lu, Y. Liu, C.T. Liu, Multicomponent intermetallic nanoparticles and superb mechanical behaviors of complex alloys, n.d. <http://science.sciencemag.org/>.
- [15] H. Peng, L. Hu, J. Chen, S. Huang, L. Li, Y. Yi, F. Zhou, W. Fang, I. Baker, Microstructures and deformation mechanisms of the medium-entropy alloy (NiCoCr)76(Ni6AlTi)3, *Mater. Sci. Eng. A* 849 (2022), <https://doi.org/10.1016/j.msea.2022.143449>.
- [16] S. Picak, J. Liu, C. Hayrettin, W. Nasim, D. Canadinc, K. Xie, Y.I. Chumlyakov, I. V. Kireeva, I. Karaman, Anomalous work hardening behavior of Fe40Mn40Cr10Co10 high entropy alloy single crystals deformed by twinning and slip, *Acta Mater.* 181 (2019) 555-569, <https://doi.org/10.1016/j.actamat.2019.09.048>.
- [17] S. Gangireddy, B. Gwalani, V. Soni, R. Banerjee, R.S. Mishra, Contrasting mechanical behavior in precipitation hardenable AlXCoCrFeNi high entropy alloy microstructures single phase FCC vs. dual phase FCC-BCC, *Mater. Sci. Eng. A* 739 (2019) 158-166, <https://doi.org/10.1016/j.msea.2018.10.021>.
- [18] P. Pandey, M. Heczko, N. Khatavkar, N. Mazumder, A. Sharma, A. Singh, M. J. Mills, K. Chattopadhyay, On the faulting and twinning mediated strengthening and plasticity in a γ' strengthened CoNi-based superalloy at room temperature, *Acta Mater.* 252 (2023), <https://doi.org/10.1016/j.actamat.2023.118928>.
- [19] P.M. Sarosi, G.B. Viswanathan, M.J. Mills, Direct observation of an extended complex stacking fault in the γ' phase of a Ni-base superalloy, *Scr. Mater.* 55 (2006) 727-730, <https://doi.org/10.1016/j.scriptamat.2006.06.019>.
- [20] B. Gwalani, S. Gangireddy, Y. Zheng, V. Soni, R.S. Mishra, R. Banerjee, Influence of ordered L1₂ precipitation on strain-rate dependent mechanical behavior in a eutectic high entropy alloy, *Sci. Rep.* 9 (2019), <https://doi.org/10.1038/s41598-019-42870-y>.

- [21] R. Glas, M. Jouiad, P. Carons, N. Clement, K. Kirchner, Order and mechanical properties of the γ matrix of superalloys, 1996.
- [22] G. Thomas, The effect of short-range order on stacking fault energy and dislocation arrangements in f.c.c. solid solutions, *Acta Metallurgica* 11 (1963) 1369–1371, [https://doi.org/10.1016/0001-6160\(63\)90035-X](https://doi.org/10.1016/0001-6160(63)90035-X), accessed September 23, 2023.
- [23] J. Miao, C. Slone, S. Dasari, M. Ghazisaeidi, R. Banerjee, E.P. George, M.J. Mills, Ordering effects on deformation substructures and strain hardening behavior of a CrCoNi based medium entropy alloy, *Acta Mater.* 210 (2021), <https://doi.org/10.1016/j.actamat.2021.116829>.
- [24] TCS High Entropy Alloys Database (TCHEA5), n.d. <https://www.thermocalc.com>.
- [25] V. Nandal, B. Harun, R. Sarvesha, S.S. Singh, E.-W. Huang, Y.-J. Chang, A.-C. Yeh, J. Jain, S. Neelakantan, Revealing the precipitation sequence with aging temperature in non-equiautomic Al_{0.2}Cr_{0.3}Fe_{0.5} high entropy alloy, *Mater. Sci. Trans. A Phys. Metall. Mater. Sci.* 53 (2022), <https://doi.org/10.1007/s11661-021-06528-7>.
- [26] S. Dasari, A. Jagetia, Y.J. Chang, V. Soni, B. Gwalani, S. Gorsse, A.C. Yeh, R. Banerjee, Engineering multi-scale B2 precipitation in a heterogeneous FCC based microstructure to enhance the mechanical properties of a Al_{0.2}Co_{1.5}Cr_{0.5}FeNi_{1.5} high entropy alloy, *J. Alloys Compd.* 830 (2020), <https://doi.org/10.1016/j.jallcom.2020.154707>.
- [27] T.T. Shun, L.Y. Chang, M.H. Shiu, Microstructures and mechanical properties of multiprincipal component CoCrFeNiTi x alloys, *Mater. Sci. Eng. A* 556 (2012) 170–174, <https://doi.org/10.1016/j.msea.2012.06.075>.
- [28] C.M. Kuo, C.W. Tsai, Effect of cellular structure on the mechanical property of Al_{0.2}Co_{1.5}Cr_{0.5}FeNi_{1.5}Ti_{0.3} high-entropy alloy, *Mater. Chem. Phys.* 210 (2018) 103–110, <https://doi.org/10.1016/j.matchemphys.2017.10.064>.
- [29] Y.J. Chang, A.C. Yeh, The formation of cellular precipitate and its effect on the tensile properties of a precipitation strengthened high entropy alloy, *Mater. Chem. Phys.* 210 (2018) 111–119, <https://doi.org/10.1016/j.matchemphys.2017.09.057>.
- [30] V. Nandal, R. Sarvesha, S.S. Singh, E.W. Huang, Y.J. Chang, A.C. Yeh, S. Neelakantan, J. Jain, Influence of pre-deformation on the precipitation characteristics of aged non-equiautomic Co_{1.5}Cr_{0.5}FeNi_{1.5} high entropy alloys with Ti and Al additions, *J. Alloys Compd.* 855 (2021) 157521, <https://doi.org/10.1016/j.jallcom.2020.157521>.
- [31] M.Z. Cao, Y. Zuo, B.B. He, Z.Y. Liang, Suppressing σ phase formation by rapid solidification to prevent embrittlement in a low-cost aged medium-entropy alloy, *J. Mater. Res. Technol.* 27 (2023) 5669–5680, <https://doi.org/10.1016/j.jmrt.2023.11.055>.
- [32] W.C. Lin, Y.J. Chang, T.H. Hsu, S. Gorsse, F. Sun, T. Furuhara, A.C. Yeh, Microstructure and tensile property of a precipitation strengthened high entropy alloy processed by selective laser melting and post heat treatment, *Addit. Manuf.* 36 (2020), <https://doi.org/10.1016/j.addma.2020.101601>.
- [33] S. Dasari, Y.J. Chang, A. Jagetia, V. Soni, A. Sharma, B. Gwalani, S. Gorsse, A. C. Yeh, R. Banerjee, Discontinuous precipitation leading to nano-rod intermetallic precipitates in an Al_{0.2}Ti_{0.3}Co_{1.5}Cr_{0.5}FeNi_{1.5} high entropy alloy results in an excellent strength-ductility combination, *Mater. Sci. Eng.* (2021) 805, <https://doi.org/10.1016/j.msea.2020.140551>.
- [34] B. Gwalani, S. Gorsse, V. Soni, M. Carl, N. Ley, J. Smith, A.V. Ayyagari, Y. Zheng, M. Young, R.S. Mishra, R. Banerjee, Role of copper on L12 precipitation strengthened fcc based high entropy alloy, *Materialia (Oxf)* 6 (2019), <https://doi.org/10.1016/j.mtla.2019.100282>.
- [35] B. Gwalani, V. Soni, D. Choudhuri, M. Lee, J.Y. Hwang, S.J. Nam, H. Ryu, S. H. Hong, R. Banerjee, Stability of ordered L12 and B2 precipitates in face centered cubic based high entropy alloys - Al_{0.3}Co_{0.3}Fe_{0.3}C_{0.1}Ni_{0.1} and Al_{0.3}Co_{0.3}Fe_{0.3}Ni_{0.1}, *Scr. Mater.* 123 (2016) 130–134, <https://doi.org/10.1016/j.scriptamat.2016.06.019>.
- [36] I.A. Su, K.K. Tseng, J.W. Yeh, B. El-Sayed, C.H. Liu, S.H. Wang, Strengthening mechanisms and microstructural evolution of ductile refractory medium-entropy alloy Hf₂₀Nb₁₀Ti₃₅Zr₃₅, *Scr. Mater.* (2022) 206, <https://doi.org/10.1016/j.jallcom.2020.156321>.
- [37] A.J. Zaddach, C. Niu, C.C. Koch, D.L. Irving, Mechanical properties and stacking fault energies of NiFeCrCoMn high-entropy alloy, *JOM* 65 (2013) 1780–1789, <https://doi.org/10.1007/s11837-013-0771-4>.
- [38] S. Qiu, X.C. Zhang, J. Zhou, S. Cao, H. Yu, Q.M. Hu, Z. Sun, Influence of lattice distortion on stacking fault energies of CoCrFeNi and Al-CoCrFeNi high entropy alloys, *J. Alloys Compd.* 846 (2020), <https://doi.org/10.1016/j.jallcom.2020.156321>.
- [39] X. Wang, C. Qiu, Effect of aging temperature on microstructure and mechanical properties of laser melted and hot isostatically pressed (CoCrFeMnNi)₉₆(TiAl)₄ alloy, *J. Alloys Compd.* 936 (2023), <https://doi.org/10.1016/j.jallcom.2022.168317>.
- [40] H. Shahmir, M.S. Mehranpour, S.A. Arsalan Shams, T.G. Langdon, Twenty years of the CoCrFeNiMn high-entropy alloy: achieving exceptional mechanical properties through microstructure engineering, *J. Mater. Res. Technol.* 23 (2023) 3362–3423, <https://doi.org/10.1016/j.jmrt.2023.01.181>.
- [41] T. Yang, Z. Tang, X. Xie, R. Carroll, G. Wang, Y. Wang, K.A. Dahmen, P.K. Liaw, Y. Zhang, Deformation mechanisms of Al_{0.1}CoCrFeNi at elevated temperatures, *Mater. Sci. Eng. A* 684 (2017) 552–558, <https://doi.org/10.1016/j.msea.2016.12.110>.
- [42] X. Wang, Y. Ding, H. Yu, Z. Bi, Y. Gao, B. Gan, High strength and ductility in a novel Ni-based superalloy with γ' and nanotwins /stacking faults architectures, *Mater. Sci. Eng. A* 847 (2022), <https://doi.org/10.1016/j.msea.2022.143293>.
- [43] H. Huang, J. Wang, H. Yang, S. Ji, H. Yu, Z. Liu, Strengthening CoCrNi medium-entropy alloy by tuning lattice defects, *Scr. Mater.* 188 (2020) 216–221, <https://doi.org/10.1016/j.scriptamat.2020.07.027>.
- [44] C. Zhang, C. Zhu, P. Cao, X. Wang, F. Ye, K. Kaufmann, L. Casalena, B. E. MacDonald, X. Pan, K. Vecchio, E.J. Lavernia, Aged metastable high-entropy alloys with heterogeneous lamella structure for superior strength-ductility synergy, *Acta Mater.* 199 (2020) 602–612, <https://doi.org/10.1016/j.jactamat.2020.08.043>.
- [45] L. Fan, T. Yang, Y. Zhao, J. Luan, G. Zhou, H. Wang, Z. Jiao, C.T. Liu, Ultrahigh strength and ductility in newly developed materials with coherent nanolamellar architectures, *Nat. Commun.* 11 (2020), <https://doi.org/10.1038/s41467-020-20109-z>.
- [46] J.H. Lee, T.B. Holland, A.K. Mukherjee, X. Zhang, H. Wang, Direct observation of Lomer-Cottrell Locks during strain hardening in nanocrystalline nickel by in situ TEM, *Sci. Rep.* 3 (2013), <https://doi.org/10.1038/srep01061>.
- [47] Y. Deng, C.C. Tasan, K.G. Pradeep, H. Springer, A. Kostka, D. Raabe, Design of a twinning-induced plasticity high entropy alloy, *Acta Mater.* 94 (2015) 124–133, <https://doi.org/10.1016/j.jactamat.2015.04.014>.
- [48] D. Kuhlmann-Wilsdorf, Theory of plastic deformation: - properties of low energy dislocation structures, *Mater. Sci. Eng.* 113 (1989) 1–41.
- [49] J.W. Christian, S. Mahajan, Deformation twinning, *Prog. Mater. Sci.* 39 (1995) 1–157.
- [50] X. Lv, F. Sun, J. Tong, Q. Feng, J. Zhang, Paired dislocations and their interactions with γ' particles in polycrystalline superalloy GH4037, *J. Mater. Eng. Perform.* 24 (2015) 143–148, <https://doi.org/10.1007/s11665-014-1307-y>.
- [51] H.C. Liu, C.M. Kuo, P.K. Shen, C.Y. Huang, H.W. Yen, C.W. Tsai, Disorderizing of L1₂ phase in high-entropy alloy deformed at cryogenic temperature, *Adv. Eng. Mater.* 23 (2021), <https://doi.org/10.1002/adem.202100564>.
- [52] R.W. Kozar, A. Suzuki, W.W. Milligan, J.J. Schirra, M.F. Savage, T.M. Pollock, Strengthening mechanisms in polycrystalline multimodal nickel-base superalloys, *Mater. Sci. Trans. A Phys. Metall. Mater. Sci.* 40 (2009) 1588–1603, <https://doi.org/10.1007/s11661-009-9858-5>.
- [53] K. Ming, X. Bi, J. Wang, Realizing strength-ductility combination of coarse-grained Al_{0.2}Co_{1.5}Cr_{0.5}FeNi_{1.5}Ti_{0.3} alloy via nano-sized, coherent precipitates, *Int. J. Plast.* 100 (2018) 177–191, <https://doi.org/10.1016/j.ijplas.2017.10.005>.
- [54] D.C. Ludwigson, Modified stress-strain relation for FCC metals and alloys, *Mater. Sci. Trans.* 2 (2) (1971) 2825–2828, <https://doi.org/10.1007/BF02813258>, accessed September 24, 2023.
- [55] V. Gerold, H.P. Karnthaler, On the origin of planar slip in f.c.c. alloys, *Acta Metallurgica* 37 (1989) 2177–2183.
- [56] Y. Liao, I. Baker, On the room-temperature deformation mechanisms of lamellar-structured Fe30Ni20Mn35Al15, *Mater. Sci. Eng. A* 528 (2011) 3998–4008, <https://doi.org/10.1016/j.msea.2011.01.089>.
- [57] Q. Li, T.W. Zhang, J.W. Qiao, S.G. Ma, D. Zhao, P. Lu, B. Xu, Z.H. Wang, Superior tensile properties of Al_{0.3}Co_{0.3}Fe_{0.3}Ni high entropy alloys with B2 precipitated phases at room and cryogenic temperatures, *Mater. Sci. Eng. A* 767 (2019), <https://doi.org/10.1016/j.msea.2019.138424>.
- [58] K. Ma, H. Wen, T. Hu, T.D. Topping, D. Isheim, D.N. Seidman, E.J. Lavernia, J. M. Schoenung, Mechanical behavior and strengthening mechanisms in ultrafine grain precipitation-strengthened aluminum alloy, *Acta Mater.* 62 (2014) 141–155, <https://doi.org/10.1016/j.jactamat.2013.09.042>.
- [59] A. Haglund, M. Koehler, D. Cattoor, E.P. George, V. Keppens, Polycrystalline elastic moduli of a high-entropy alloy at cryogenic temperatures, *Intermetallics (Barking)* 58 (2015) 62–64, <https://doi.org/10.1016/j.intermet.2014.11.005>.